energies

MDPI

Article

Structural Optimization and Test Analysis of Hot Platen in Small-Scale Laminator

Shuzhen Li, Boda Song, Jianshu Li, Liang Zhang *, Lei Shi and Jiale He

College of Mechanical and Electrical Engineering, Hebei Normal University of Science & Technology, Qinhuangdao 066001, China; lsz3320@hevttc.edu.cn (S.L.); 17732105276@163.com (B.S.); 13832436736@163.com (J.L.); shileihnust@sina.com (L.S.); lejiahh@163.com (J.H.)
* Correspondence: liang1053@hevttc.edu.cn

Abstract

To address the temperature non-uniformity of heating platens in small-scale photovoltaic (PV) module laminators, this study develops a wire-wound hot platen with a Square loop layout and arithmetic-progression wire spacing. The heating wires are represented by an equivalent surface-heat-flux boundary, and CFD simulations are used to evaluate the effects of wiring layout, wire length, and spacing on the temperature field. The optimized Square loop layout reduces the full-field working-surface-temperature standard deviation from 1.887 °C to 0.552 °C, a reduction of 70.8%. A FLUENT-UDF incremental PID model is then developed using the top-surface area-weighted average temperature as feedback. At the 4800 s endpoint, the simulated controlled average is 150.55 °C, with a steady-state error of +0.55 °C and a maximum positive deviation of approximately 0.96 °C at approximately 4480 s; the holding-stage response shows a small limit-cycle oscillation of approximately ±1 °C. The local center-point temperature T_1 is 153.0 °C, indicating a center-to-edge spatial non-uniformity that is distinct from the controller overshoot. A small-scale laminator platform with 13 thermocouples was used to benchmark the simulated platen-level temperature field. The measured 13-point average temperature is 150.55 °C, the maximum temperature difference is 3.0 °C, and the 13-point sample standard deviation is 1.05 °C; the maximum absolute error and mean absolute error are 1.30 °C and 0.913 °C, respectively. These results support the proposed surface-heat-flux model and incremental PID design for small laminator hot platens under the tested platen-level conditions.

Keywords: laminator; structural design; CFD simulation; PID temperature control

Check for updates

Academic Editor: Artur Blaszczuk

Received: 3 September 2026
Revised: 12 October 2026
Accepted: 13 October 2026
Published: 16 October 2026

Copyright: © 2026 by the authors. Licensee MDPI, Basel, Switzerland. This article is an open access article distributed under the terms and conditions of the Creative Commons Attribution (CC BY) license.

1. Introduction

The photovoltaic (PV) industry, as a cornerstone of the clean energy transition, relies heavily on the technological advancement of its key equipment for high-quality growth [1,2]. The PV module laminator is a core piece of equipment in the module encapsulation process, where the performance of the heating platform directly determines the cross-linking degree of the ethylene–vinyl acetate (EVA) encapsulant, the bonding quality between layers, and ultimately, the overall power generation efficiency of the module [3–5]. Existing research has explored various technical approaches to enhance heating performance. For instance, Zhang et al. [6] investigated a factory-provided silicone rubber heating plate, establishing a theoretical thermal conductivity model based on heat-transfer theory. Their experimental validation demonstrated that the average error between simulation and experiment was within ±2.6 °C, confirming the model's feasibility and providing a theoretical reference for

manufacturing engineering. Furthermore, Muneeshwaran and Wang [7] demonstrated that optimizing the thermal design of a bake station, specifically by employing funnel-shaped baffles, reducing the baffle angle, and introducing an air gap between the lid and the hot plate, could significantly improve temperature uniformity during the post-exposure bake process for wafers. Both experimental and numerical analyses confirmed that these modifications effectively optimized air-flow distribution and reduced heat loss, achieving a remarkably low temperature non-uniformity of only 0.2–0.3 °C across a 6-inch wafer. Similarly, Jin et al. [8] proposed a novel method to enhance temperature uniformity in induction heating by optimizing the bottom profile of the hot plate. Through numerical simulation and orthogonal experimental analysis, they found that removing material from high magnetic flux density regions on the plate's underside could effectively reshape the magnetic field distribution, thereby significantly improving surface temperature uniformity. Their results showed that the temperature difference across the target surface was reduced from approximately 9 °C to about 3 °C, meeting industrial standards. Additionally, they observed that, within the process temperature range of 140 °C to 240 °C, higher target temperatures resulted in a smaller achievable temperature non-uniformity index.

Despite growing attention to poor temperature uniformity and challenging dynamic temperature control in small-scale laminator heating platforms [9,10], existing research remains insufficient in elucidating the multi-physics coupling mechanisms of 'structure-heat transfer-control' and in achieving systematic optimization.

To further clarify the technical characteristics and inherent limitations of different hot-plate technical solutions, the mainstream heating technologies for photovoltaic laminators and related research on numerical simulation–control coupling are reviewed below.

Silicone rubber heating plates are thin, lightweight and easy to assemble, making them suitable for equipment retrofit scenarios. Optimizing the heat source layout can improve the plate temperature field to some extent; however, limited by the thermal conductivity of the silicone matrix, local hot spots tend to occur under high-power conditions, and long-term high-temperature service carries a risk of aging and delamination [11]. Thermal oil circulation heating is a mature mainstream solution for industrial PV laminators, achieving good temperature uniformity over large plates and satisfying the stress–temperature coordinated process requirements for module lamination [12]. However, this system requires oil pumps, heat exchangers and circulation pipelines, resulting in large equipment volume, complex maintenance and large thermal inertia, which makes it unsuitable for the development of small compact prototypes.

Electromagnetic induction heating has attracted attention due to its non-contact energy transfer, small thermal inertia and fast heating response. Temperature uniformity can be improved through coil configuration optimization and edge insulation, but the controller cost is high and the coil heat source can hardly achieve a continuous gradient power density distribution [9]. Shi et al. conducted induction heating research on small laminators, establishing an electromagnetic–thermal coupling model. Through coil-turn compensation combined with insulation measures, they achieved steady-state temperature control of 150 $\pm$ 2 °C on the hot plate, but the coil structure was complex [9]. Wang et al. further showed, in their simulation study of induction heating components, that, constrained by the skin effect, heat is concentrated in the metal surface layer, easily forming a temperature gradient along the thickness direction. It is difficult for coil adjustment alone to completely eliminate the temperature non-uniformity of large flat plates, which hinders the achievement of high-precision uniform temperature over the entire plate surface [13]. Traditional tubular resistance heating presses heating tubes into plate holes, with tube–matrix contact thermal resistance and discrete heat source positions, making it difficult to finely control the in-plane heat flux distribution.

Numerical simulation is an important means for predicting and optimizing the hot-plate temperature field. Park et al. conducted CFD thermal design numerical research on a large-area integrated heating/cooling hot-plate for nanoimprint lithography, evaluating the influence of plate structure on temperature distribution through simulation and providing a simulation approach for structural optimization of large-area hot plates [14]. However, in that work, thermal simulation and temperature-control were independent of each other, and no real-time two-way interaction between the control algorithm and the heat-transfer field was realized within the CFD solution loop. To link the control algorithm with the fluid heat-transfer solution, Bhujbal et al. embedded a temperature-control algorithm into the CFD simulation environment, achieving closed-loop simulation calculation of furnace internal temperature [15]. However, their object was a cavity-type heating furnace rather than a flat hot platen, and no adaptation was carried out for the multi-stage stepped heating process required for PV lamination. Most existing PV hot plate studies still treat heating-plate structural simulation and temperature control algorithm tuning separately: first completing steady-state temperature field structural optimization, and then conducting separate PID parameter experimental debugging. Few studies embed PID control logic into CFD iterative solving to dynamically evaluate the influence of the entire heating process on hot plate temperature uniformity.

Although existing studies have made certain progress in hot-plate structural layout simulation, optimization of various heating schemes, and temperature-control algorithm tuning, several shortcomings remain for the development of hot-platens for small-scale PV module laminators. First, most existing optimization work focuses on large industrial-grade laminator equipment; systematic research on wire-groove-embedded wire-wound heating-plates for small prototype scenarios is relatively scarce. Second, heating-plate structural optimization and temperature control are often studied independently; most studies report only steady-state simulation of heating-element layout or offline PID parameter tuning. Few studies embed an incremental PID algorithm into the CFD solver through a UDF to achieve two-way coupling between the control logic and the heat-transfer field. This gap makes it difficult to reproduce the dynamic temperature evolution under multi-stage heating processes. Third, many heating-layout optimizations remain at the numerical simulation stage and lack physical prototype machining and multi-point temperature measurement, so their practical engineering effectiveness on small equipment has not been adequately evaluated. In alignment with the specific process requirements for PV module lamination, this study proposes the design of a small-scale wire-wound electric heating platform. Based on CFD methods, the temperature field distribution is simulated to optimize the heating-wire layout and material selection, and an incremental PID control algorithm is introduced to achieve precise temperature control. First, taking a 600 mm $\times$ 600 mm small-scale laminator hot platen as the research object, a Square loop wiring scheme with arithmetic-progression spacing is proposed. Through gradient adjustment of the wiring spacing, the plate surface heat power density distribution is reconstructed to compensate for edge heat dissipation loss and improve working-surface temperature uniformity. Second, based on FLUENT software(2022 R1), a CFD–incremental PID coupled simulation model is built. Using UDF, the linkage between the control algorithm and heat-transfer solving is realized, and the influence of multi-stage stepped heating process curves on the hot plate dynamic temperature field is investigated. Finally, a physical heating plate prototype is machined, and a small semi-automatic laminator test platform is built. A 13-point temperature measurement scheme is adopted to complete simulation–experiment data benchmarking, and the engineering performance of the Square loop layout with arithmetic-progression spacing and the tuned PID control parameters is evaluated. This

work is expected to provide a design reference for the development of high-performance PV lamination equipment.

2. Structure and Working Principle of the Photovoltaic Module Laminator

2.1. Overall Structure of the Machine

The heating platen assembly has overall dimensions of 600 mm × 600 mm × 40 mm (length × width × height). The structural configuration of the laminator is illustrated in Figure 1; the machine comprises several core subsystems, including the heating, vacuum, pressing, and control systems, as well as feeding and cooling mechanisms. Among these, the heating system supplies the thermal energy required for lamination. As the core component of the laminator, the wire-wound heating platform features dedicated wire grooves with a depth of 1.5 mm, as depicted in Figure 2. The rated heating power of the platform is 2092 W. The heating platform is manufactured from Q235 carbon steel (Hebei Huaxi Iron and Steel Co., Ltd., Tangshan, China) and uses nickel–chromium alloy (Cr20Ni80) electric heating wires (Taizhou Yuqiang Electric Heating Appliance Technology Co., Ltd., Taizhou, China). The thermophysical properties of the materials are summarized in Table 1.

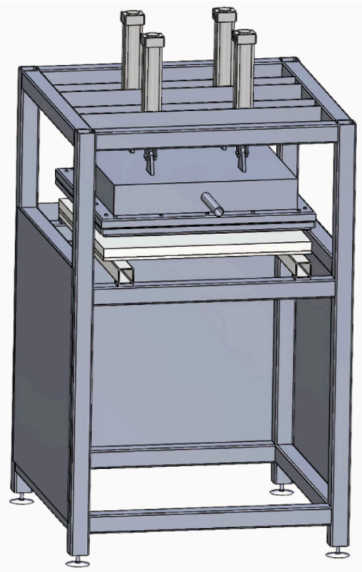


Figure 1. Overall structural drawing of photovoltaic module laminator.

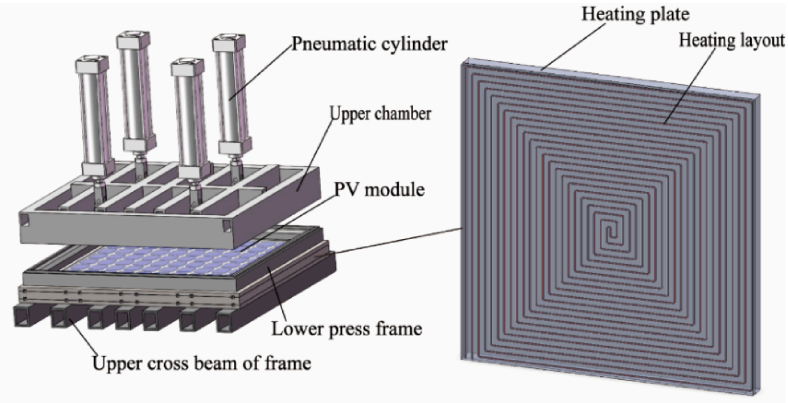


Figure 2. Structural model of the layered-winding heating platform.

Table 1. Thermophysical properties of the materials used in the heating platform.

Materials	Density (kg/m^3)	Thermal Conductivity W/(m·K)	Specific Heat Capacity J/(kg·K)
Q235	7850	50.5	465
Cr20Ni80	8100	12.5	450

2.2. Working Principle of the Laminator

The lamination process for the photovoltaic (PV) module is illustrated in Figure 3. The cycle initiates with the loading and lid-closing stages. Once the raw materials—comprising glass, EVA film, solar cells, and the backsheet—are correctly positioned, the chamber is sealed. Subsequently, vacuum pumping and heating are performed synchronously to establish the necessary conditions for the subsequent pressing phase. Once the target vacuum level and temperature are achieved, the system enters the pressing stage. This is followed by a holding phase, during which both pressure and vacuum are strictly maintained. This critical step facilitates the flow of the EVA encapsulant, effectively expelling internal air bubbles and ensuring a hermetic seal across all layers. Following the pressure and vacuum holding phase, the chamber is vented to release the pressure. Upon completion of the venting process, the lid is opened to extract the encapsulated module. The module is then cooled before being discharged, thereby completing the cycle and preparing the equipment for the encapsulation of the next PV module.

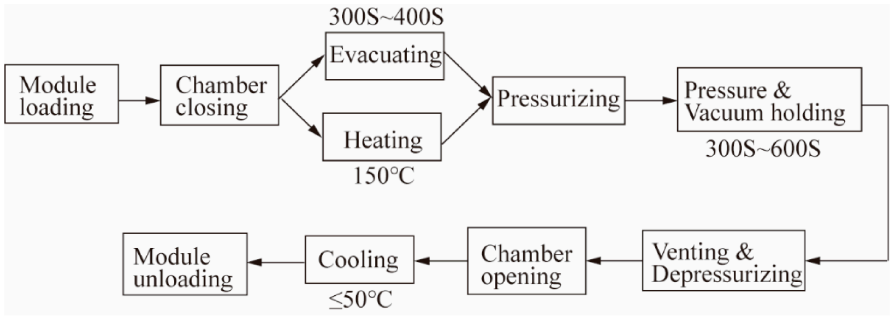


Figure 3. Lamination process of the photovoltaic module.

During the preheating stage, which involves the synchronous vacuum pumping and heating process following the closure of the lid, the heating platform is required to rapidly reach the designated operating temperature and subsequently transition into a thermal insulation state. This rapid thermal response is essential for enhancing overall temperature uniformity. Concurrently, the lower pressing frame serves to maintain the correct alignment of the stacked materials during the loading phase. It also mates with the upper housing to form a hermetically sealed chamber, thereby ensuring the smooth execution of critical processes such as vacuum evacuation.

2.3. Theoretical Analysis of Heating Platform Heat Transfer

The heat-transfer mechanisms of the heating platform mainly involve thermal conduction and natural convection. In the actual lamination process, the electric heating elements transfer thermal energy to the PV module primarily by conduction. Once the preset temperature is reached, heat is conducted through the thermal insulation blocks to the frame, establishing a stable temperature gradient. In the air-based simulation, natural convection between the platform, the frame, and the surrounding air is also considered and significantly influences the overall thermal equilibrium.

(1) Thermal conduction: Thermal conduction facilitates energy transfer through lattice vibrations of molecules or atoms, as well as the movement of free electrons within a medium. The efficiency of this heat transfer is intrinsically determined by the material's properties. Consequently, the design of the heating platform must carefully account for the impact of thermal contact resistance at heterogeneous material interfaces and anisotropic thermal conductivity on the uniformity of the temperature field [16].

The rate of heat conduction is governed by the material's thermal conductivity, the temperature gradient, and the geometric configuration of the object. Utilizing Fourier's Law, the heat flux across different sections of the heating platform can be quantified [17]. The mathematical formulation for one-dimensional steady-state heat conduction is expressed as:

$$q = -k \cdot A \cdot \frac{\Delta T}{L} \tag{1}$$

where q is the heat flow rate (J/s), k is the thermal conductivity (W/(m·K)), A is the cross-sectional area perpendicular to the heat flow (m^2), ΔT is the temperature difference (°C), and L is the length of the heat-transfer path (m).

(2) Thermal convection: Thermal convection involves the transfer of heat through the macroscopic movement of a fluid (gas or liquid). The surrounding fluid environment significantly influences the heat dissipation efficiency of the heating platform. Convective heat transfer can be quantified using Newton's Law of Cooling, where the convective heat-transfer coefficient (h) is dependent on various factors, including the thermophysical properties of the fluid, flow velocity, and surface roughness [18].

The formula for the convective heat-transfer rate is expressed as:

$$q = h \cdot A \cdot \Delta T \tag{2}$$

where h is the convective heat-transfer coefficient, A is the surface area of the heating platform (m^2), and ΔT is the temperature difference (°C).

(3) The temperature field, T(x,y,z,t), of the heating platform satisfies the heat conduction equation [19,20]:

$$\rho c_p \frac{\partial T}{\partial t} = \nabla (k \nabla T) \tag{3}$$

where ρ is the material density (kg/m^3), c_p is the specific heat capacity (J/(kg·K)), and k is the thermal conductivity (W/(m·K)). The wire heating is imposed as a surface-flux boundary and is therefore not included as a volumetric source term in Equation (3). The heat source within the electric heating platform is determined by the Joule heating generated as an electric current passes through the conductor. The corresponding expression is given by:

$$P = I^2 R \tag{4}$$

where P is the total heating power of the electric heating wires (W), I is the current (A), and R is the total electrical resistance (Ω).

In the simulation calculation, the electric heating wires are represented as a surface heat-flux boundary. The equivalent surface heat-flux density is adopted:

$$q = \frac{P}{A_h} \tag{5}$$

where q is the uniform surface heat-flux density on the outer surfaces of the electric heating wires (W/m^2), A_h is the total outer surface area of the wire-equivalent boundary zone (m^2), and P is the total heating power (W). The value A_h = 0.307643045 m^2 is extracted from the wire-equivalent CAD/mesh surface and excludes the upper and lower groove surfaces. In

FLUENT, the wire outer faces are selected as a boundary thread, and the UDF assigns q uniformly to all faces in that thread.

Convective boundary condition on the outer surfaces outside the resolved air domain is given by:

$$-k\frac{\partial T}{\partial n} = h(T - T_\infty) \quad (6)$$

where h is the convective heat-transfer coefficient ($W/(m^2 \cdot K)$), and T_∞ is the ambient temperature (K). Equation (6) is applied only to the outer surfaces outside the resolved air domain and is not applied to the heated working surface, which is treated as a coupled wall.

The initial condition is defined as:

$$T(x, y, z, 0) = T_0(x, y, z) \quad (7)$$

where $T_0(x, y, z)$ is the initial temperature distribution (K).

The specific implementation of the equivalent joule heating in FLUENT is as follows. The electric heating wires are represented by their outer surfaces rather than by a solid conductor domain. The wire-equivalent surface zone is selected as a boundary thread, and a DEFINE_PROFILE UDF assigns $q = P/A_h$ to every face in that thread. The total power is therefore conserved over the sum of the wire outer-surface areas, while the spatial distribution of the heat input follows the wire layout. Other solid domains receive no external heat flux. The remaining platen surfaces exchange heat with the resolved air domain through coupled walls, and natural convection is resolved within the air domain. The prescribed convective boundary condition with h is applied only to the outer surfaces outside the resolved air domain.

3. Simulation Analysis and Optimization of Heat-Transfer Characteristics of the Heating Platform

3.1. Establishment of the Physical Model for the Heating Platform

Based on the structural configuration and operating principles of the heating apparatus, a three-dimensional model of the heating platform was established. Non-critical structural components such as load-bearing beams, bolts, and threaded holes were omitted to reduce computational cost. The electric heating wires were not resolved as an internal conductor domain; instead, their outer surfaces were represented by a surface heat-flux boundary, as described in Section 2.3. The resulting simplified model is illustrated in Figure 4.

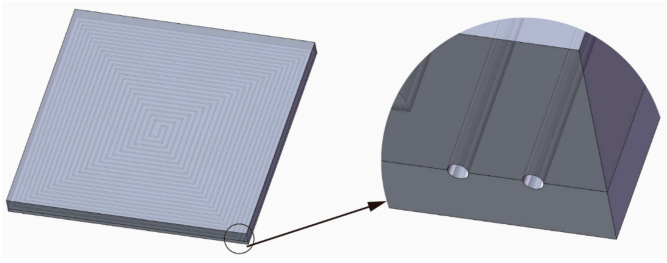


Figure 4. Simplified model of heating platform.

3.2. Boundary Conditions

The encapsulation of photovoltaic (PV) modules requires the heating platform to be preheated, a process that typically takes approximately 60 min. The initial ambient temperature was set to 24 °C, and the boundaries of the air domain were configured as constant-temperature walls at 24 °C. This setup facilitates heat exchange between the internal air and the boundaries, thereby simulating the actual experimental environment.

The working surface and other platen surfaces were defined as coupled walls, so heat is exchanged with the resolved air domain by conjugate heat transfer; no prescribed convective heat-transfer coefficient was applied to the heated working surface. The boundary conditions applied to the air domain are illustrated in Figure 5. To accurately capture the heat transfer between the heating apparatus and the surrounding air, a flow field encompassing the heating platform was established.

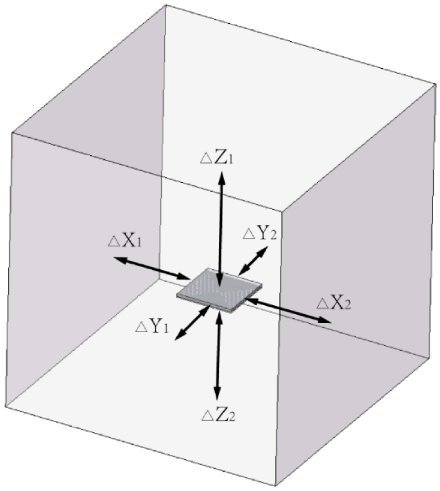


Figure 5. Boundary conditions of the air domain of the heating platform.

The dimensions of this computational domain are defined as $\Delta x_1 = \Delta x_2 = 1.2$ m, $\Delta y_1 = \Delta y_2 = 1.2$ m, $\Delta z_1 = 2.0$ m, and $\Delta z_2 = 1.0$ m.

The distance from the outer boundary of the air domain to the hot plate is at least one hot-plate edge length in each direction (hot-plate footprint: 600 mm × 600 mm). This domain size reduces the artificial influence of far-field boundaries on the natural-convection flow around the hot plate. There is no forced blowing in the experimental environment; only natural convection is enabled in the simulation, so the simulation boundary conditions are consistent with the actual laboratory conditions.

Solver settings. A pressure-based transient solver was used. Gravity was enabled, and buoyancy in the resolved air domain was represented using the Boussinesq approximation with reference temperature $T_0 = 297.15$ K, reference density $\rho_0 = 1.185$ kg/m^3, and thermal expansion coefficient $\beta = 1/360 \approx 2.78 \times 10^{-3}$ K^{-1}. The time step was 1 s, consistent with the PID sampling interval. The scaled residual convergence criteria were 1×10^{-3} for continuity and momentum and 1×10^{-6} for energy, with a maximum of 20 iterations per time step. The outer boundaries of the air domain were set as constant-temperature walls at 24 °C. The working surface and other platen surfaces were treated as coupled walls exchanging heat with the resolved air domain. A convective heat-transfer coefficient $h = 8$ W/(m^2·K) was prescribed only on the outer surfaces outside the resolved air domain and was not imposed on the heated working surface. This value represents natural convection in still air and does not include thermal radiation.

3.3. Mesh Generation and Independence Verification

A flow field model of the air domain surrounding the heating platform was established. The air-side heat-transfer coefficient was evaluated during post-processing from the resolved flow and temperature fields and was not imposed as a boundary condition on the working-surface heat-transfer coefficient, and an unstructured mesh was generated for the heating platform. To ensure the reliability and accuracy of the numerical simulation results, a grid independence test was conducted to eliminate the potential influence of

mesh density on the simulation outcomes [21]. Maintaining identical boundary conditions, an automatic meshing method was utilized to generate six meshes of varying densities by adjusting the element size. The total number of mesh elements for these cases were 490,000, 1.19 million, 1.69 million, 2.13 million, 2.65 million, and 3.03 million, respectively. The variation in the average heat flux across the working surface of the heating platform was selected as the evaluation metric to perform a comparative analysis of the relative errors. The corresponding results are summarized in Table 2.

Table 2. Grid-independence verification results.

Number of Grids (10^4)	Average Heat Flux (W/m^2)	Deviation (%)
49	588.7738	---
119	581.0374	1.31%
169	577.8879	0.54%
213	580.5152	0.45%
265	582.6742	0.37%
303	580.7033	0.34%

Applicability of the Boussinesq approximation. The Boussinesq approximation is adopted as a first-order buoyancy closure for the resolved air domain. For the present temperature range (24–150 °C), the buoyancy parameter is $\beta\Delta T \approx 0.35$ and the density ratio between 24 and 150 °C is about 0.70, so the approximation is not in the strict small-perturbation limit. The purpose of the present model is to capture the average convective boundary condition rather than the detailed local air-flow structure. Previous studies of large-temperature-difference air convection have shown that the average heat flux and average Nusselt number are much less sensitive to property variations than the local velocity and temperature fields [22]. Chenoweth and Paolucci [23] found that the average heat flux is essentially unchanged even when the local fields are strongly affected, and a comparison of Boussinesq and real-air-density models reported a maximum difference of 0.436% in the average Nusselt number for air with ΔT up to 200 K [24]. In the present configuration, the working-surface temperature field is dominated by conduction in the steel platen and the heating-wire layout, while air-side convection acts as a boundary loss. The Boussinesq model is therefore considered adequate for the present comparative study, whose conclusions are based on the solid-side temperature field, the layout ranking, and the PID control performance.

The grid independence test procedure is illustrated in Figure 6.

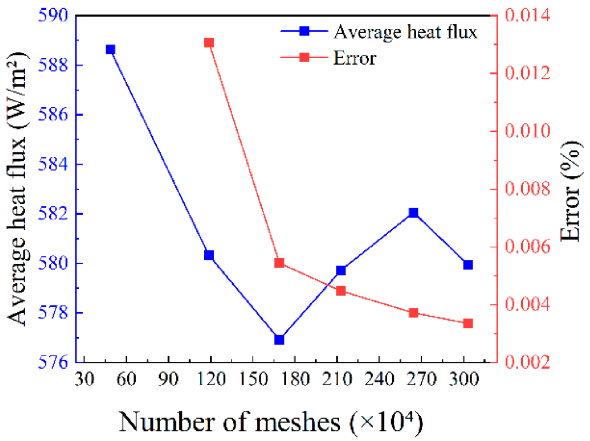


Figure 6. Diagram of the grid-independence verification process.

The analysis results indicate that, as the number of mesh elements increases from 490,000 to 1.69 million, the average heat flux of the heating platform decreases gradually, and the relative deviation drops from 1.31% to 0.54%. This indicates that mesh density markedly affects the simulation results. When the mesh count is further increased to 2.13–3.03 million, the average heat flux fluctuates within a narrow band of 580.5–582.7 W/m^2, and the relative deviation remains between 0.34% and 0.45%. Mesh sensitivity has therefore become negligible in this range. Considering the trade-off between simulation accuracy and computational efficiency, and the temperature-field and flow-field characteristics around the heating platform, a mesh comprising 2.13 million elements was selected for this study.

3.4. Analysis of the Influence of the Layout Shape of the Electric Heating Wire

The three heating-wire layouts evaluated in this study are denoted as the S-Shaped layout, the Combined layout, and the Square loop layout. Their schematic diagrams are presented in Figure 7. In the CFD model, the spatial distribution of the surface heat-flux boundary follows the positions of the wire outer surfaces; therefore, changing the winding spacing changes the spatial distribution of the heat input even when the total heating power and total wire-surface area remain unchanged. CFD simulations were conducted to evaluate the influence of these layouts on the temperature field [25,26]. The resulting temperature contours are presented in Figure 8, and the corresponding temperature parameters are summarized in Table 3. In terms of temperature uniformity, the layouts are ranked as Square loop layout > Combined layout > S-Shaped layout [27]. The influence of heating-element layout on heat transfer and temperature uniformity has also been reported for other heating configurations [28].

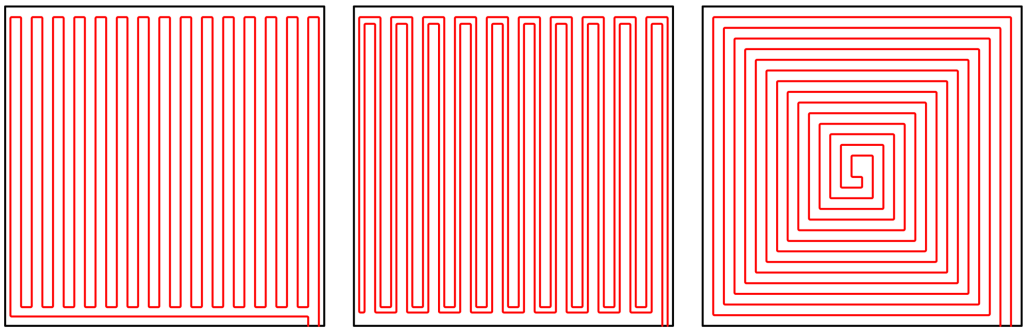


Figure 7. Schematic diagrams of the three heating-wire layouts: (**a**) S-Shaped layout, (**b**) Combined layout, and (**c**) Square loop layout.

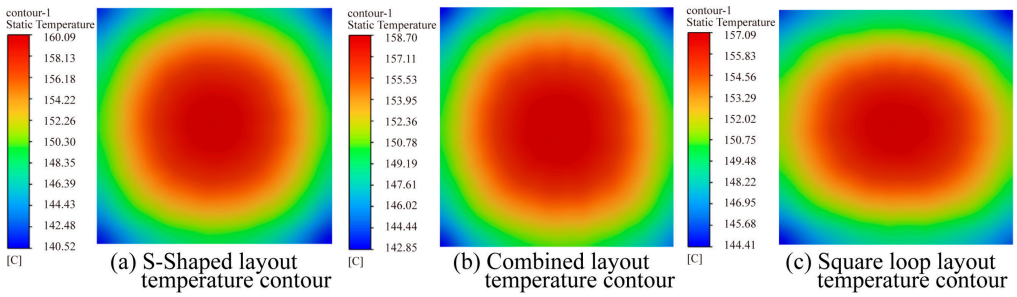


Figure 8. Temperature contours of the heating platform for the three heating-wire layouts.

Table 3. Temperature uniformity indicators of the three heating-wire layouts.

Heating-Wire Layout	Max. Temp. (°C)	Min. Temp. (°C)	Max. Temp. Diff. (°C)	Avg. Temp. (°C)	TSD (°C)
S-Shaped layout	160.09	140.52	19.57	152.80	4.290
Combined layout	158.70	142.85	15.85	152.77	3.554
Square loop layout	157.09	144.41	12.68	152.73	2.742

3.5. Effect of Heating-Wire Length on Temperature Uniformity

To analyze the influence of heating-wire length on the platen temperature field, five heating platforms with different wire lengths and spacings were considered based on the plate size and the conventional equal-spacing Square loop layout, with the same total power. The optimal heating-wire length was determined by comparing the maximum temperature difference and temperature standard deviation on the upper surface. The wire-length and spacing settings and the corresponding simulation results are given in Table 4.

Table 4. Parameters and simulation results for heating wires of different lengths.

Scheme	Wire Length (mm)	Spacing (mm)	Max. Plate Temp. Diff. (°C)	Plate Temp. Std. Dev	Avg. Temp. (°C)	Heating Time (s)	TNU (%)
1	14,469	23.00	12.68	2.742	152.731	3600	8.30
2	16,536	20.30	11.50	2.473	152.840	3600	7.52
3	19,280	17.60	10.84	2.309	152.971	3600	7.09
4	23,150	14.80	9.61	2.061	153.168	3600	6.27
5	28,940	11.95	8.79	1.887	153.481	3600	5.73

The heating times in Tables 4 and 5 refer to the constant-power design simulations without PID control.

Table 5. Effects of arithmetic-progression spacing on the temperature uniformity of the Square loop layout.

First Term (mm)	Common Difference (mm)	Max. Plate Temp. Difference (°C)	Plate Temp. Std. Dev	Heating Time (s)
10.00	0.25	4.44	1.014	3496
10.25	0.22	3.17	0.697	3532
10.50	0.19	3.52	0.552	3494
10.75	0.15	3.89	0.552	3532
11.00	0.12	4.54	0.703	3494

For the conventional equal-spacing Square loop wiring, as the heating-wire length increases from 14.47 m to 28.94 m, the working-surface-temperature standard deviation decreases from 2.742 °C to 1.887 °C. Under the same heating time and total power, Scheme provides the best temperature uniformity. Considering the simulation results and manufacturing feasibility, a heating-wire length of 28.94 m was selected. The variation in the working-area temperature difference with heating-wire length is shown in Figure 9, and the temperature contours of the five platforms are shown in Figure 10.

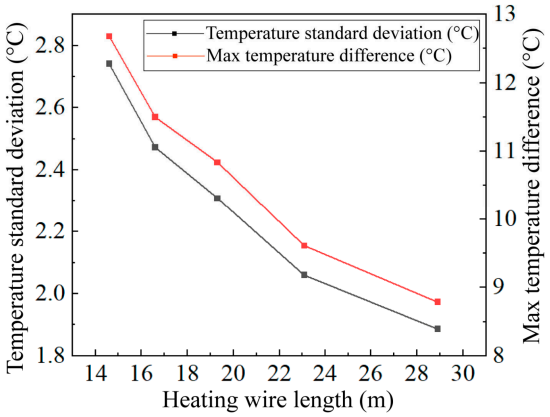


Figure 9. Temperature difference in the working area of the heating platform corresponding to different heating-wire lengths.

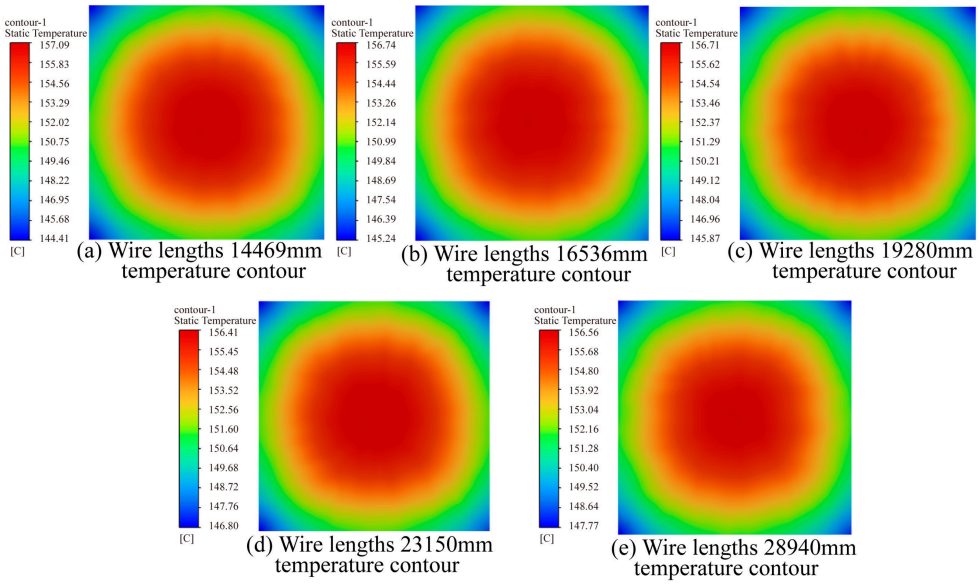


Figure 10. Temperature contours of the heating platform for five different heating-wire lengths.

3.6. Effect of Heating-Wire Spacing on Temperature Uniformity

Loop layout with arithmetic-progression spacing is illustrated in Figure 11. The arithmetic-progression spacing schemes and their simulation results are summarized in Table 5. The relevant parameter settings in FLUENT are the same as in Section 3.4. In addition, the temperature contours for each scheme are presented in Figure 12.

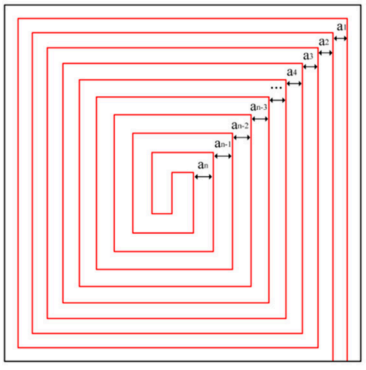


Figure 11. Schematic diagram of the Square loop layout with arithmetic-progression spacing.

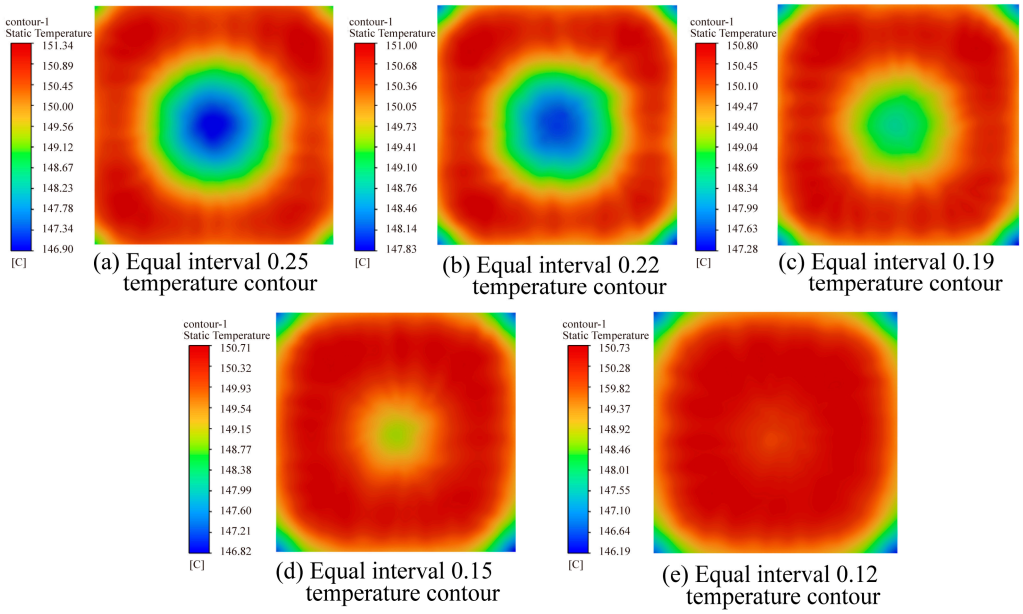


Figure 12. Temperature contours of the Square loop layout with different arithmetic-progression spacing schemes.

The simulation results demonstrate that, with an initial spacing of 10.50 mm and a common difference of 0.19 mm, the standard deviation of the working-surface temperature is reduced from 1.887 °C to 0.552 °C, representing a 70.8% improvement in temperature uniformity. Consequently, a heating-wire scheme with a total length of 28.94 m and an appropriately matched wire diameter was ultimately selected.

Comparing the results in Table 5, the two schemes with first term 10.50 mm/common difference 0.19 mm and first term 10.75 mm/common difference 0.15 mm yield the same working-surface-temperature standard deviation of 0.552 °C, but differ in maximum temperature difference and heating time. The 10.50 mm/0.19 mm scheme has a plate maximum temperature difference of 3.52 °C and a heating time of 3494 s, while the 10.75 mm/0.15 mm scheme has a maximum temperature difference of 3.89 °C and a heating time of 3532 s. Under the same temperature standard deviation, the 10.50 mm/0.19 mm scheme has a smaller plate maximum temperature difference and a shorter heating time, balancing extreme-value temperature uniformity and heating efficiency; therefore, these parameters are selected for the final heating-wire layout. The baseline temperature standard deviation of 1.887 °C is the simulation result of the conventional equal-spacing Square loop layout and is used to quantitatively evaluate the optimization effect of arithmetic-progression spacing in the Square loop layout.

From the perspective of the heat-transfer physical mechanism, the convective heat dissipation loss at the hot-plate edges is significantly higher than that in the central region. With conventional equal-spacing Square loop wiring, heat accumulates in the center while edge temperatures are lower. The arithmetic-progression spacing strategy arranges the heating wire more densely as the edge is approached, increasing the heat source power density per unit area in the edge region to compensate for convective heat dissipation; meanwhile, the central wiring spacing is moderately increased to reduce central heat input. This matches the plate surface heat input with the heat dissipation loss, thereby improving the overall working-surface temperature uniformity.

4. Incremental PID Temperature-Control Simulation Analysis

4.1. Principle of Incremental PID Temperature Control

The temperature-control process of the heating platform comprises two distinct phases: dynamic heating and steady-state thermal insulation. An incremental PID algorithm is employed to achieve closed-loop temperature control. By calculating both the current and historical errors, the incremental PID determines the adjustment increment for the heat source power through proportional, integral, and derivative operations [29]. Continuous modulation of the heat source power enables precise temperature regulation of the heating platform, thereby satisfying the stringent thermal requirements during the insulation phase. The logical diagram of the PID control system is presented in Figure 13.

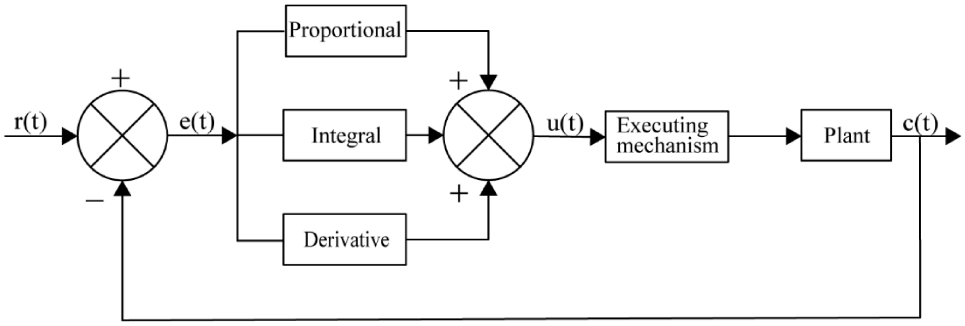


Figure 13. PID control logic flowchart.

Heat source power increment:

$$\Delta P(k) = K_p[e(k) - e(k-1)] + K_i e(k) + K_d[e(k) - 2e(k-1) + e(k-2)] \quad (8)$$

Heat source power at the next step:

$$P(k) = P(k-1) + \Delta P(k) \quad (9)$$

where $\Delta P(k)$ is the power increment in W at step k; e(k), e(k − 1), and e(k − 2) are the current, previous, and two-step-earlier temperature errors in °C; Kp = 45 W/°C, Ki = 10 W/(°C·step), and Kd = 0.5 W·step/°C are the incremental PID gains; P(k) is the total heating power in W; and the sampling step is 1 s.

The required heat source power for the next control cycle is obtained by adding the calculated power increment to the current heat source power. Through this mechanism, the system can continuously modulate the heat source power in response to real-time temperature variations, thereby achieving precise temperature control of the heating platform.

In this simulation, the PID sampling interval is equal to the FLUENT time step of 1 s. The controlled variable is the area-weighted average temperature of the working surface, obtained from the FLUENT report definition 'ave'. This quantity represents the average temperature of the heated working surface and is not the local center-point temperature T_1. The heat source power is limited to the range 0–2092 W. The incremental PID gains are Kp = 45 W/°C, Ki = 10 W/(°C·step), and Kd = 0.5 W·step/°C. The controller starts with P(0) = 2092 W and updates the power at the end of each time step.

4.2. Simulation Analysis of Temperature Field Under Incremental PID Temperature Control

In this study, the FLUENT User-Defined Function (UDF) uses DEFINE_EXECUTE_AT_END to read the report definition 'ave' at the end of each time step, calculate the incremental PID update, and store the new total heating power. The heat input is applied by DEFINE_PROFILE on the outer faces of the electric heating wires. For every

face in the selected thread, the UDF assigns the same surface heat-flux density $q = P(k)/A_h$, where A_h is the total outer surface area of the wire-equivalent boundary zone. The value of A_h is obtained from the CAD/mesh geometry and excludes the upper and lower groove surfaces. This approach conserves the prescribed total power over the wire outer surfaces and preserves the spatial layout of the heat input.

Through engineering commissioning, the incremental PID gains were selected as Kp = 45 W/°C, Ki = 10 W/(°C·step), and Kd = 0.5 W·step/°C. The target profile applies setpoints of 60, 90, 120, and then 150 °C at 0, 1000, 2000, and 3000 s, respectively. Because the controller regulates the working-surface average temperature, T_1 is treated as a local center-point indicator rather than the controlled variable.

The target temperature is set to 60 °C from 0 s to 1000 s, increases to 90 °C from 1000 s to 2000 s, and rises to 120 °C from 2000 s to 3000 s. Beyond 3000 s, the target temperature is maintained at 150 °C. The control code is shown in Figure 14.

```
/* 1. Set target temp (multi-segment profile) */
if (tim1 < 1000)
    set_temp = 60.0;   // Target 60℃ from 0 to 1000s
else if (tim1 < 2000)
    set_temp = 90.0;   // Target 90℃ from 1000 to 2000s
else if (tim1 < 3000)
    set_temp = 120.0;  // Target 120℃ from 2000 to 3000s
else if (tim1 < 4000)
    set_temp = 150.0;  // Target 150℃ from 3000 to 4000s
else
    set_temp = 150.0;  // Target 150℃ after 4000s
```

Figure 14. PID temperature-control code.

The target temperature–time command applied to the incremental PID controller in this study is a stepped holding heating mode: from 0 to 1000 s, the target temperature is 60 °C and held; from 1000 to 2000 s, the target temperature is 90 °C and held; from 2000 to 3000 s, the target temperature is 120 °C and held; after 3000 s, the target temperature is 150 °C and held. The controller maintains the corresponding set temperature within each time interval, and this temperature command corresponds one-to-one with the temperature variation curve in Figure 16. The final setpoint of 150 °C is applied at t = 3000 s, and the simulation is advanced to t = 4800 s. The controlled area-weighted average first reaches 150 °C at approximately 3834 s. All contour and time-history results in this section correspond to this 0–4800 s simulation.

The temperature contours on the working surface at the end of the final heating step and at the 4800 s endpoint of the final setpoint interval are presented in Figure 15. At 4800 s, the controlled working-surface average is 150.55 °C, the 13-point sample standard deviation is about 1.28 °C, the maximum temperature difference is 4.1 °C, and the center-point temperature T_1 is 153.0 °C. The positive deviation of T_1 is a local spatial non-uniformity effect; it is not a controller overshoot because the PID feedback variable is the working-surface average.

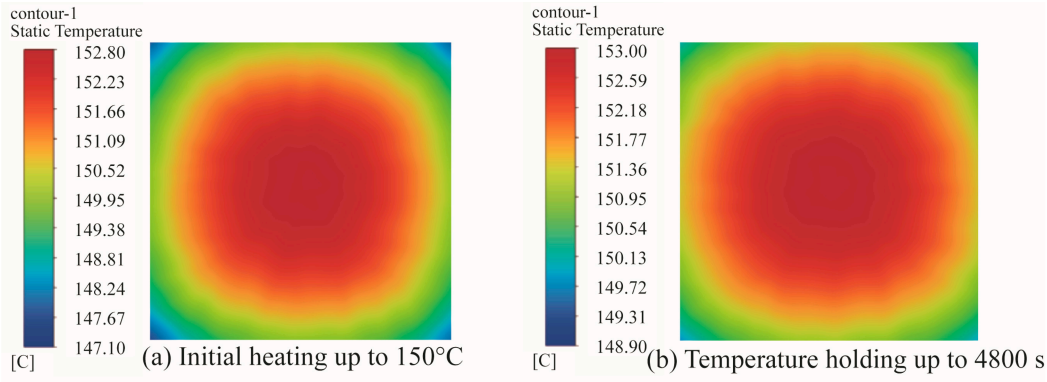


Figure 15. Simulated temperature contours of the heating platform at the end of the holding phase.

Figure 16 shows the time history of the controlled area-weighted average temperature at three scales: (a) the full heating process, (b) the initial heating stage, and (c) the holding stage. The controlled average is 149.64, 150.10, and 150.55 °C at 3600, 4200, and 4800 s, respectively. Because panel (a) uses a 0–200 °C axis, the small holding-stage oscillation is below its visual resolution; panels (a) and (c) show the same controlled average at different scales. The controlled average first reaches 150 °C at approximately 3834 s, and the simulation record ends at 4800 s. The local monitor T_1 is reported in Tables 7 and 10; The final setpoint interval extends from 3000 to 4800 s, and the 4800 s endpoint is used consistently for Figure 15b, Figure 16c and Figure 20.

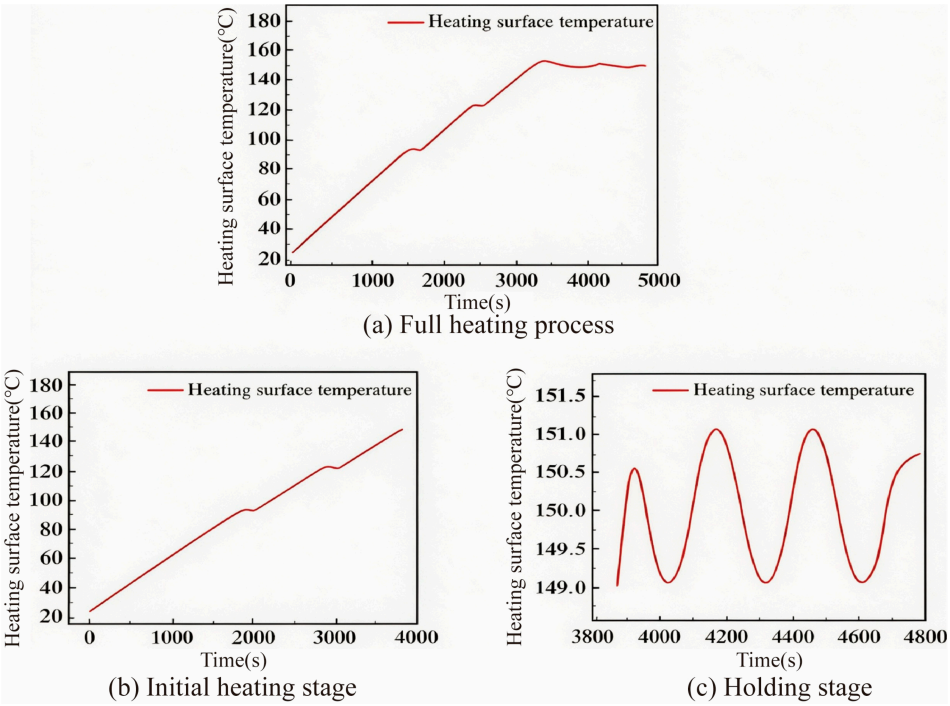


Figure 16. Controlled area-weighted average temperature of the Square loop layout: (**a**) full heating process; (**b**) initial heating stage; (**c**) holding stage. Panels (**a**,**c**) show the same quantity at different temperature scales; the holding-stage oscillation is resolved only in (**c**). The stepped setpoints are 60, 90, 120 and 150 °C at 0, 1000, 2000 and 3000 s.

The simulation results show that the incremental PID controller stabilizes the working-surface average temperature while the local center point remains hotter than the average. Overshoot is defined as the maximum positive deviation of the controlled average above 150 °C after the final setpoint change at 3000 s. Steady-state error is defined as the difference

between the controlled average and 150 °C at 4800 s. The nominal holding duration is 1800 s from 3000 to 4800 s. The maximum positive deviation of the controlled average after the 150 °C setpoint change is approximately 0.96 °C, occurring at approximately 4480 s. The holding-stage response also shows a limit-cycle oscillation of approximately ±1 °C, and the steady-state error at the 4800 s endpoint is +0.55 °C. These values refer to the controlled average and must not be inferred from the local T_1 value.

5. Experiments and Analysis

5.1. Experimental Materials and Equipment

The physical prototypes of the heating platform and the small-scale semi-automatic laminator are illustrated in Figure 17. The main body of the heating platform is fabricated by welding two layers of Q235 carbon structural steel, featuring overall dimensions of 600 mm × 600 mm × 40 mm. Semi-circular wire grooves with a depth of 1.5 mm and a diameter of 3 mm are machined within both the upper and lower plates. Nickel–chromium alloy electric heating wires are embedded within these grooves, as depicted in Figure 17a.

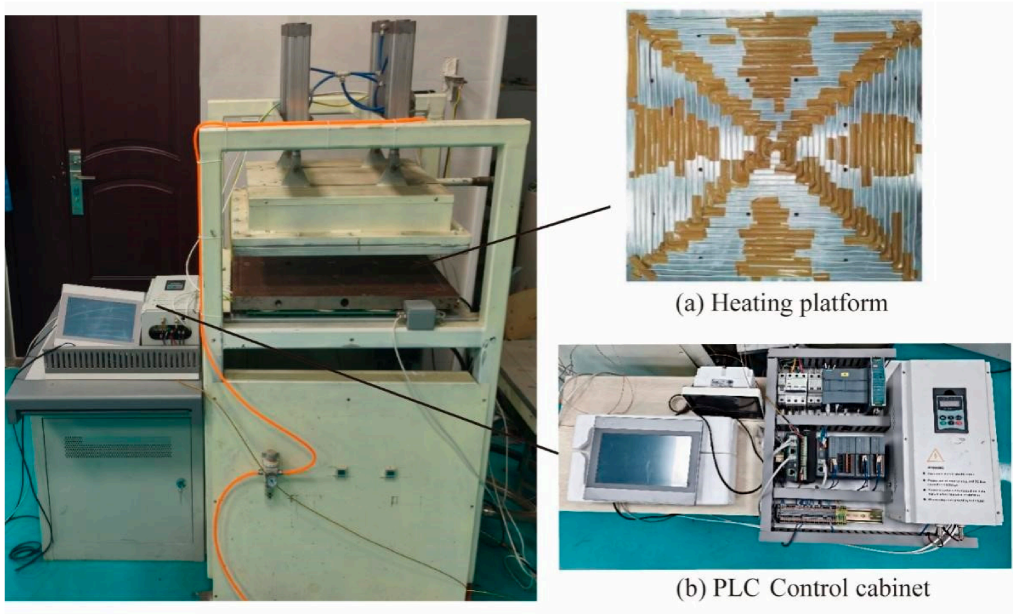


Figure 17. Photographs of the layered-winding heating platform and the small-scale semi-automatic laminator.

The experimental setup comprises a multi-channel data logger equipped with data recording capabilities and K-type thermocouples. The multi-channel data logger is utilized to acquire multiple temperature signals and simultaneously display the temperatures at various points across the laminator. K-type thermocouples, employing contact-type temperature probes, are deployed to monitor the temperature variations at specific locations within the laminator. The layered-winding electric heating platform is regulated by a PID control cabinet, which serves as the core control system, as illustrated in Figure 17b. The K-type thermocouples, multi-channel temperature recorder, K-type thermocouple compensation wires and electric heating wires used in the experiment are shown in Figure 18.

5.2. Experimental Method

The nickel–chromium electric heating wires were connected to the power and temperature-control modules of the laminator control cabinet. The control cabinet used a surface-temperature signal from its own temperature-control module as the experimental feedback variable; however, its location, number, and raw time series were not recorded, so

the absolute experimental steady-state error cannot be reconstructed. The 13 thermocouples were therefore used only for temperature-field validation, and T_1 was retained as the local center-point monitor. The setpoint profile was 60, 90, 120, and 150 °C from 0, 1000, 2000, and 3000 s onward, respectively; the final setpoint interval extended from 3000 to 4800 s. Both the simulation and the experiment were recorded to 4800 s, and the controlled average first reached 150 °C at approximately 3834 s in the simulation.

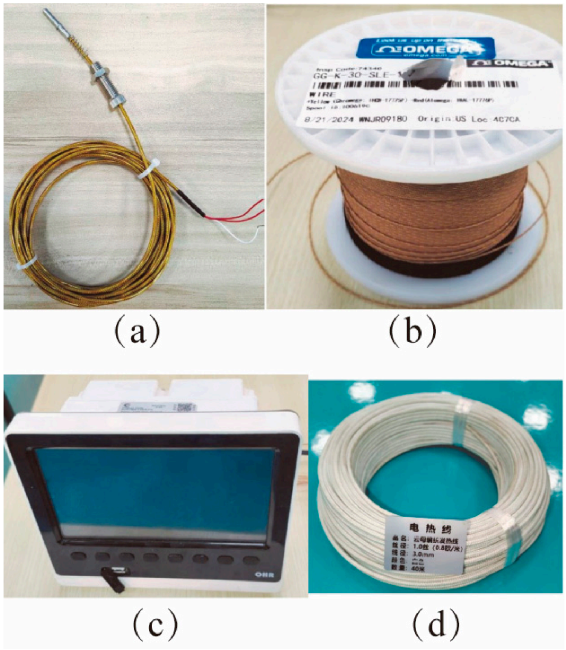


Figure 18. Equipment for temperature measurement tests. (**a**) K-type thermocouples; (**b**) Compensation wires; (**c**) Multi-channel temperature recorder; (**d**) Electric heating wires.

In this experiment, 13 K-type thermocouples (T_1–T_{13}) were arranged over the 600 mm × 600 mm hot plate with the upper-left corner as the coordinate origin. T_1 was located at (300, 300) mm, i.e., the geometric center, and served as the local center-point monitor. The horizontal and vertical spacing between adjacent measurement positions was 125 mm, and the outermost measurement positions were 50 mm from the plate edges. T_2–T_9 captured corner and edge effects, whereas T_{10}–T_{13} represented the transition regions between the center and edges. The 13 measured points were used to estimate the experimental temperature-field average and spatial uniformity and were not treated as the control-cabinet feedback signal. The measurement layout is shown in Figure 19.

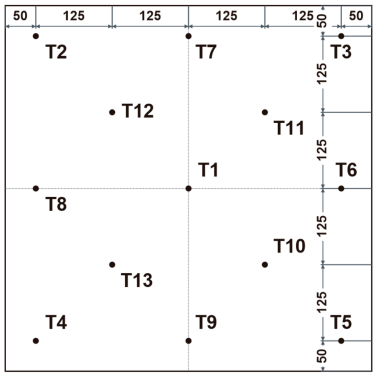


Figure 19. Schematic diagram of temperature measurement point locations.

All 13 K-type thermocouples were calibrated before the experiment following National Metrological Specification of China [30]. A secondary standard platinum resistance thermometer with U = 0.05 °C (k = 2) was used with a high-precision thermostatic oil bath whose working-zone axial uniformity was no greater than 0.02 °C and whose temperature fluctuation within 10 min was no greater than 0.01 °C. The standard thermometer and each tested thermocouple were inserted into a copper isothermal block to reduce conduction and radiation errors. Calibration points of 50, 100, and 150 °C covered the heating and holding ranges. At each point, 10 readings were recorded at 10 s intervals. The arithmetic mean of the standard-thermometer readings defined the reference temperature, and linear interpolation was used to establish the correction curve over 50–150 °C. The indicated errors of all 13 thermocouples were within ±0.3 °C, satisfying the B-grade K-type thermocouple requirement.

The Type B uncertainty components were estimated from the stated maximum permissible errors of the K-type thermocouples (±0.5 °C) and the multi-channel recorder (±0.2 °C). Because the manufacturers did not specify an error distribution, these limit values were conservatively treated as standard uncertainties with k = 1, rather than converted using a rectangular distribution. The calibration standard (U = 0.05 °C, k = 2 → u = 0.025 °C) and the oil-bath non-uniformity and fluctuation (≤0.02 and ≤0.01 °C) were included as additional small Type B components. The Type B components were combined by the root-sum-square method: $u_B = \sqrt{(0.5)^2 + (0.2)^2} = \sqrt{0.29} \approx 0.54$ °C. Each condition was repeated three times. At 4800 s, the sample standard deviations of the three repetitions across the 13 measurement points ranged from 0.12 to 0.26 °C, with a mean of 0.19 °C. The sample standard deviation, rather than the standard error of the mean, was used as the Type A standard uncertainty, which is conservative. The Type A standard uncertainty is:

$$u_A = s = \sqrt{\frac{1}{n-1}\sum_{i=1}^{n}(x_i - \overline{x})^2} \tag{10}$$

The Type A and Type B components were combined by the root-sum-square method:

$$u_c = \sqrt{u_A^2 + u_{B1}^2 + u_{B2}^2 + u_{cal}^2 + u_{bath}^2} \tag{11}$$

The combined standard uncertainty is therefore u_c = 0.57 °C. The value 0.57 °C is the combined standard uncertainty and must not be labeled as the expanded uncertainty.

Taking k = 2 for an approximate 95% confidence level gives the expanded measurement uncertainty:

$$U = ku_c \tag{12}$$

The expanded measurement uncertainty is U = 1.14 °C (k = 2).

The measurement-uncertainty budget is summarized in Table 6.

Table 6. Measurement-uncertainty budget.

Source	Type	Value	Standard Uncertainty
Repeatability (3 runs, 13 points)	A	0.12–0.26 °C, mean 0.19	0.19 °C
K-type thermocouple MPE	B	±0.5 °C	0.50 °C
Multi-channel recorder MPE	B	±0.2 °C	0.20 °C
Calibration standard	B	U = 0.05 °C, k = 2	0.025 °C
Oil-bath uniformity/fluctuation	B	≤0.02/0.01 °C	0.018 °C
Combined standard uncertainty			0.57 °C
Expanded uncertainty (k = 2)			1.14 °C

5.3. Results and Discussion

The simulated working-surface temperature field at the 4800 s endpoint of the final setpoint interval is presented in Figure 15. The same figure is referenced here to avoid duplicating the temperature-contour result. The temperatures at the 13 measurement points at 600, 1200, 1800, 2400, 3000, 3600, 4200, and 4800 s are summarized in Table 7. The final holding interval from 3000 to 4800 s is therefore represented by eight sampled time points.

Table 7. Simulated local temperatures at the 13 measurement points.

Time/s	Temperature Measurement Points/°C												
	T_1	T_2	T_3	T_4	T_5	T_6	T_7	T_8	T_9	T_{10}	T_{11}	T_{12}	T_{13}
600	48.1	44.4	44.5	46.8	47.0	45.0	45.1	45.1	47.3	44.6	47.0	47.7	47.6
1200	71.5	67.4	67.1	69.4	69.6	68.2	68.5	68.4	70.4	67.6	69.7	71.1	71.0
1800	94.1	89.3	89.3	91.4	91.6	90.7	91.0	91.0	92.8	89.8	91.7	93.5	93.4
2400	115.6	110.8	110.6	112.5	112.7	112.1	112.4	112.4	114.0	111.2	112.8	114.7	114.6
3000	136.4	131.3	130.9	132.6	132.6	132.7	133.1	133.0	134.3	131.7	132.8	135.1	135.0
3600	152.8	147.6	147.1	148.5	148.7	149.5	150.1	150.0	150.8	148.1	148.8	151.7	151.6
4200	152.8	148.2	148.1	149.5	149.6	149.8	150.4	150.4	151.0	148.5	149.5	151.8	151.7
4800	153.0	148.9	148.9	149.9	150.1	150.3	150.8	150.7	151.3	149.1	150.0	152.1	152.0

Through testing of the temperature field on the working surface of the heating platform, the temperatures at each measurement point at 600 s, 1200 s, 1800 s, 2400 s, 3000 s, 3600 s, 4200 s and 4800 s were recorded, and the temperature data are summarized in Table 8.

Table 8. Measured temperatures at the thirteen measurement points on the working surface.

Time/s	Temperature Measurement Points/°C												
	T_1	T_2	T_3	T_4	T_5	T_6	T_7	T_8	T_9	T_{10}	T_{11}	T_{12}	T_{13}
600	46.8	45.7	45.8	45.7	45.8	46.2	46.4	46.3	46.1	45.9	45.8	46.5	46.4
1200	70.3	68.6	68.4	68.3	68.4	69.4	69.7	69.6	69.2	68.8	68.5	69.9	69.8
1800	93	90.5	90.5	90.4	90.5	91.8	92.2	92.1	91.7	91	90.6	92.4	92.3
2400	114.6	111.8	111.7	111.6	111.7	113.1	113.5	113.4	113	112.2	111.8	113.7	113.6
3000	135.5	132.2	131.8	131.8	131.8	133.6	134	133.9	133.5	132.6	132	134.3	134.2
3600	152.1	148.3	147.9	147.9	148	150.2	150.8	150.7	150.1	148.8	148.1	151	150.9
4200	152.2	148.9	148.8	148.9	149	150.5	151.1	151	150.4	149.2	148.9	151.2	151.1
4800	152.4	149.5	149.5	149.4	149.6	150.9	151.4	151.3	150.8	149.7	149.5	151.6	151.5

The thermocouple probes were attached to the working surface with high-temperature-resistant thermal adhesive, and the sampling interval was 2 s. The final result for each condition was the arithmetic mean of three repetitions after applying the calibration corrections. The three-repeat measurements at 4800 s are listed in Table 9.

To evaluate the accuracy of the established PID temperature-control model, 13 measurement points (T_1–T_{13}) on the arithmetic-spacing heating platform were tested. The temperature difference between the center and edge regions affects module warpage and yield [31,32], so T_1–T_5 were selected as representative points for the comparison in Figure 20. The statistical error analysis in Section 5.3 uses all 13 measurement points.

The maximum absolute error between the simulation and experimental data is 1.30 °C, and the maximum relative error is below 3%. The relative error decreases significantly as the temperature rises. After reaching the steady state (i.e., beyond 4200 s), the relative errors at all measurement points drop below 0.6%. The prototype experiment benchmarks the simulated temperature field only for the Square loop layout with arithmetic-progression

spacing, thereby evaluating the numerical model and PID parameters for that configuration; the conventional equal-spacing Squart was tested experimentally.

Table 9. Three repeated measurements at 4800 s and sample standard deviations.

Point	Run 1	Run 2	Run 3	Mean	Sample SD
T_1	152.20	152.40	152.60	152.40	0.20
T_2	149.25	149.50	149.75	149.50	0.25
T_3	149.24	149.50	149.76	149.50	0.26
T_4	149.16	149.40	149.64	149.40	0.24
T_5	149.37	149.60	149.83	149.60	0.23
T_6	150.70	150.90	151.10	150.90	0.20
T_7	151.20	151.40	151.60	151.40	0.20
T_8	151.10	151.30	151.50	151.30	0.20
T_9	150.60	150.80	151.00	150.80	0.20
T_{10}	149.58	149.70	149.82	149.70	0.12
T_{11}	149.38	149.50	149.62	149.50	0.12
T_{12}	151.48	151.60	151.72	151.60	0.12
T_{13}	151.38	151.50	151.62	151.50	0.12

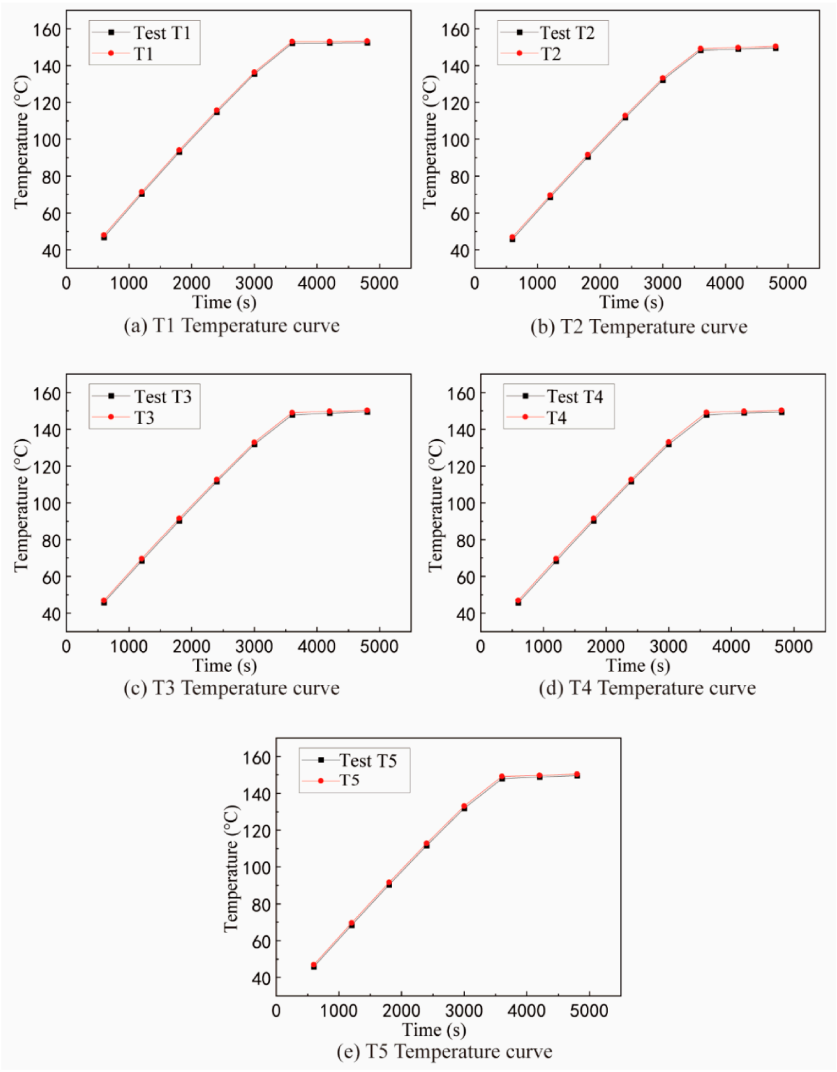


Figure 20. Comparison between simulated and experimental temperatures at the five measurement points.

Grid-independence verification addresses numerical discretization error and is not equivalent to experimental validation of the CFD physical model. To evaluate the prediction capability of the CFD model, 104 simulation–experiment pairs from 13 measurement points and 8 time instants were analyzed: the maximum absolute error is 1.30 °C, the mean absolute error is MAE = 0.913 °C, the root mean square error is RMSE = 0.948 °C, and the coefficient of determination is R^2 = 0.999. The maximum relative error is 2.84%. These metrics are based on the rounded values reported in Tables 7 and 8. The combined standard uncertainty was 0.57 °C, and the expanded measurement uncertainty was 1.14 °C (k = 2). The MAE of 0.913 °C was smaller than this expanded uncertainty, whereas the maximum absolute error of 1.30 °C was slightly larger than it. These differences are therefore of the same order as the measurement uncertainty under the tested conditions, without implying validation of untested layouts or full vacuum lamination.

At 4800 s, the measured 13-point average temperature is 150.55 °C, the sample standard deviation is 1.05 °C, the maximum temperature difference is 3.0 °C, and the center point T1 is 152.4 °C. The corresponding simulation values are a controlled area-weighted surface average of 150.55 °C, a 13-point arithmetic mean of 150.55 °C, a 13-point sample standard deviation of 1.28 °C, a maximum temperature difference of 4.1 °C, and T_1 = 153.0 °C. The measured 13-point arithmetic mean and the simulated area-weighted controlled average agree closely, but the experimental control-cabinet feedback signal was not recorded, so the absolute experimental control error cannot be calculated. The 13-point values are also not directly equivalent to the full-field CFD standard deviation of 0.552 °C obtained in the no-PID layout-optimization model. Table 10 summarizes these control-performance metrics and clearly separates the simulated feedback variable, the unrecorded control-cabinet signal, the 13-point average temperature, and the local center point.

For clarity, the CFD full-field temperature standard deviation is defined as:

$$\sigma_T = \sqrt{\left(\int_A (T - \overline{T})^2 dA / A \right)} \tag{13}$$

where A is the working-surface area.

The 13-point sample standard deviation is defined as:

$$s_T = \sqrt{(\sum_i (T_i - \overline{T}) / (n - 1))} \tag{14}$$

where n = 13.

The full-field CFD value of 0.552 °C and the 13-point sample values of 1.28 °C (simulation) and 1.05 °C (experiment) are therefore different statistical quantities and are not directly interchangeable.

Table 10. Control performance summary at the 4800 s endpoint of the final setpoint interval.

Metric	Simulation	Experiment
Closed-loop feedback variable	Area-weighted average temperature of the top working surface	Control-cabinet surface-temperature signal (not recorded)
Controlled-variable value at 4800 s	150.55 °C	Not available
13-point average temperature at 4800 s	150.55 °C	150.55 °C
Center point T1 at 4800 s	153.0 °C	152.4 °C
Maximum surface temperature difference at 4800 s	4.1 °C	3.0 °C
13-point sample standard deviation at 4800 s	1.28 °C	1.05 °C
Maximum positive deviation after the 150 °C setpoint (3000–4800 s)	≈0.96 °C at ≈4480 s	Not comparable

Table 10. *Cont.*

Metric	Simulation	Experiment
Holding-stage oscillation amplitude	≈±1 °C	Not comparable
Steady-state error of the controlled variable at 4800 s	+0.55 °C	Not available
Expanded measurement uncertainty (k = 2)	Not applicable	±1.14 °C
Combined standard uncertainty (k = 1)	Not applicable	0.57 °C

6. Conclusions

This study investigated the thermal design, surface-heat-flux modeling, and incremental PID control of a wire-wound heating platform for a small-scale photovoltaic module laminator. The main conclusions are as follows:

(1) A CFD thermal-design model of the wire-wound heating platform was established by representing the electric heating wires as uniform surface heat-flux boundaries. Among the compared layout types, the Square loop layout provided the best temperature uniformity. With arithmetic-progression spacing in the Square loop layout, the full-field working-surface-temperature standard deviation decreased from 1.887 °C to 0.552 °C, corresponding to a 70.8% numerical reduction. These results demonstrate that spacing redistribution can effectively compensate for edge heat loss and improve the thermal uniformity of the small platen.

(2) A CFD-UDF incremental PID model was established with the top-surface area-weighted average temperature as the closed-loop feedback variable. The controlled average reached 150.55 °C at the 4800 s endpoint, with a steady-state error of +0.55 °C and a maximum positive deviation of approximately 0.96 °C at approximately 4480 s within the 3000–4800 s interval. The holding-stage response exhibited a small limit-cycle oscillation of approximately ±1 °C. The local center point T1 reached 153.0 °C, indicating a center-to-edge spatial non-uniformity that is distinct from the controller overshoot.

(3) A small-scale semi-automatic laminator test platform and a 13-point thermocouple measurement system were constructed. At 4800 s, the measured 13-point average temperature was 150.55 °C, the maximum temperature difference was 3.0 °C, the 13-point sample standard deviation was 1.05 °C, and T1 was 152.4 °C. These measurements were consistent with the predicted temperature level and the local center-to-edge distribution of the optimized Square loop layout.

(4) The simulation and experimental temperature fields showed close agreement. For 104 paired data points from 13 measurement positions and 8 time instants, the maximum absolute error was 1.30 °C, the mean absolute error was 0.913 °C, the root mean square error was 0.948 °C, the maximum relative error was 2.84%, and the coefficient of determination was R^2 = 0.999. The combined standard uncertainty was 0.57 °C, and the expanded measurement uncertainty was 1.14 °C (k = 2); the mean absolute difference was within this uncertainty, while the maximum absolute difference was comparable to it. These results support the reliability of the established surface-heat-flux and control model under the tested operating conditions.

(5) The study establishes an engineering workflow that integrates equivalent surface-heat-flux modeling, wiring-layout optimization, UDF-based incremental PID control, and multi-point experimental benchmarking. For the tested 600 mm × 600 mm platen and 150 °C lamination condition, the Square loop layout with arithmetic-progression spacing provides a practical reference for improving temperature uniformity in small-scale photovoltaic module laminators. Extension to full vacuum lamination, industrial-scale platens, and other process temperatures remain objectives for future work.

7. Limitations and Prospects

This study has several limitations: (1) the prototype temperature measurement uses 13 thermocouples, which cannot fully characterize the continuous spatial temperature field of the 600 mm × 600 mm working surface; (2) only the Square loop layout with arithmetic-progression spacing was tested physically, so the 70.8% improvement over the equal-spacing Square loop layout remains a simulation result; (3) the CFD model represents the platen assembly in air and does not include the laminated PV stack, applied pressure, vacuum pumping, or surface-to-surface radiation; (4) the electric heating wires are represented by a surface heat-flux boundary rather than a conductor model with explicit Joule heating; (5) the control-cabinet feedback signal, including its sensor position and raw time series, was not recorded, so the experimental absolute steady-state error cannot be independently evaluated; (6) the 4800 s record is shorter than a full production hold at 150 °C, and a longer hold test is required for full process qualification; (7) the measurement-uncertainty budget is based on a conservative treatment of manufacturer error limits and repeatability data and does not cover every environmental and installation effect; (8) machining tolerances of the grooved winding may change the actual wire spacing and thermal performance; and (9) the Boussinesq approximation may not reproduce the local air-flow structure at the largest temperature difference, and a full variable-density cross-check was not possible because the original case and data files are no longer available.

Future work should record the control-cabinet feedback signal and sensor location, perform physical A/B tests of Square loop plates with equal and arithmetic-progression spacing, evaluate a variable-density air model, add a vacuum- and radiation-coupled model with a loaded PV stack, extend the holding test beyond the present 4800 s record, and refine the measurement-uncertainty budget by including environmental and installation effects.

Author Contributions: Conceptualization, S.L.; methodology, S.L., L.S. and L.Z.; software, J.H.; formal analysis, B.S. and J.L.; investigation, B.S., J.L. and J.H.; resources, S.L., L.Z. and L.S.; data curation, B.S., J.L. and J.H.; writing—original draft preparation, B.S., J.L. and J.H.; writing—review and editing, S.L., L.S. and L.Z.; supervision, L.Z. and L.S. All authors have read and agreed to the published version of the manuscript.

Funding: This research received no external funding.

Data Availability Statement: The original contributions presented in the study are included in the article, further inquiries can be directed to the corresponding author.

Acknowledgments: This study extends its sincere gratitude to all individuals who provided valuable insights and suggestions.

Conflicts of Interest: The authors declare that no commercial or financial relationships that could be construed as a potential conflict of interest existed during the conduct of this study.

Abbreviations

CFD	Computational fluid dynamics
Cr20Ni80	Nickel–chromium resistance-heating alloy (80% Ni, 20% Cr)
EVA	Ethylene–vinyl acetate
MAE	Mean absolute error [°C]
PID	Proportional–integral–derivative
PV	Photovoltaic
Q235	Chinese carbon structural steel grade 235
R^2	Coefficient of determination
RMSE	Root mean square error [°C]
SD	Standard deviation [°C]

TNU	Temperature non-uniformity
TSD	Temperature standard deviation [°C]
UDF	User-defined function
Avg. Temp.	Average temperature
Max. Temp.	Maximum temperature
Min. Temp.	Minimum temperature
Max. Temp. Diff.	Maximum temperature difference

References

1. Sraisth, S. Achieving faster lamination process for crystalline photovoltaic modules by using latest lamination technologies. In Proceedings of the 33rd European Photovoltaic Solar Energy Conference and Exhibition, Amsterdam, The Netherlands, 25–29 September 2017; pp. 992–997.
2. Alimi, O.A.; Meyer, E.L.; Olayiwola, O.I. Solar photovoltaic modules' performance reliability and degradation analysis—A review. *Energies* **2022**, *15*, 5964. [CrossRef]
3. Zeng, F.; Guo, X.; Sun, L.; He, X.; Zeng, Z.; Liu, Z. Non-isothermal crosslinking of ethylene vinyl acetate initiated by crosslinking agents: Kinetic modelling. *RSC Adv.* **2022**, *12*, 15623–15630. [CrossRef] [PubMed]
4. Li, H.Y.; Théron, R.; Röder, G.; Turings, T.; Luo, Y.; Lange, R.F.; Ballif, C.; Perret-Aebi, L.-E. Insights into the Encapsulation Process of Photovoltaic Modules: GC-MS Analysis on the Curing Step of Poly (ethylene-co-vinyl acetate)(EVA) Encapsulant. *Polym. Polym. Compos.* **2012**, *20*, 665–672. [CrossRef]
5. Öz, A.K.; Reichel, C.; Wellens, C.; Mittag, M.; Heinrich, M.; Neuhaus, D.H. Simulation and experimental analysis of temperature profiles and crosslinking in PV module lamination. *IEEE J. Photovolt.* **2024**, *14*, 777–784. [CrossRef]
6. Zhang, Y.; Lu, W.; Wang, M.; Qian, Y. Analysis of Temperature Field of Silicone Heating Plate based on COMSOL. *Recent Pat. Mech. Eng.* **2024**, *17*, 2–10. [CrossRef]
7. Muneeshwaran, M.; Wang, C.C. Thermal design aspects for improving temperature homogeneity of silicon wafer during thermal processing in microlithography. *Appl. Therm. Eng.* **2020**, *171*, 115118. [CrossRef]
8. Jin, W.; Xing, C.; Lu, Y.; Baoshou, S.; Li, D. A novel method improving the temperature uniformity of hot-plate under induction heating. *Proc. Inst. Mech. Eng. Part C J. Mech. Eng. Sci.* **2021**, *235*, 190–201. [CrossRef]
9. Shi, L.; Liu, Y.; Duan, P.; Zhang, L.; Li, A. Optimization of Temperature Uniformity in Photovoltaic Laminators Based on Electromagnetic Induction Heating. *Energies* **2025**, *18*, 6096. [CrossRef]
10. Guan, L.M.; Tian, J.X.; Chen, L.; Zhang, W. Study on Temperature Control System of Film Laminating Machine. *Appl. Mech. Mater.* **2013**, *397–400*, 1263–1270. [CrossRef]
11. Ni, S.; Lu, W.; Wang, J. Optimization of the temperature field and design for enhancing uniform temperature distribution in silicone heating plates. *Recent Pat. Mech. Eng.* **2025**, *19*, 1–8. [CrossRef]
12. Zheng, J.; Hou, G. Introduction to the Heat Transfer Oil System. *Process Equip. Pip.* **2012**, *49*, 31–33.
13. Wang, J.; Hou, Q.; Wang, F.; You, B.; Yuan, H.-Y. Simulation and analysis of the heating performance of an embossing-head utilizing electromagnetic induction heating. *Trans. FAMENA* **2021**, *45*, 101–113. [CrossRef]
14. Park, G.; Lee, C. Numerical study on thermal design of a large-area hot plate with heating and cooling capability for thermal nanoimprint lithography. *Appl. Sci.* **2019**, *9*, 3100. [CrossRef]
15. Bhujbal, S.; Andhale, A.; Deshpande, A.; Pimpalnerkar, S. Implementation of Control Algorithm for Furnace Temperature Control in CFD Simulation. In *Proceedings of the 2016 International Conference on Automatic Control and Dynamic Optimization Techniques (ICACDOT)*; IEEE: New York, NY, USA, 2016; pp. 110–113. [CrossRef]
16. Jiji, L.M. *Heat Conduction*; Springer: Berlin/Heidelberg, Germany, 2009. [CrossRef]
17. Abd-Elhady, M.S.; Abdelhady, S. A new approach for formulating the transport phenomena. *Int. Commun. Heat Mass Transf.* **2026**, *172*, 110602. [CrossRef]
18. Zhao, B. Integrity of Newton's cooling law based on thermal convection theory of heat transfer and entropy transfer. *Sci. Rep.* **2022**, *12*, 16292. [CrossRef] [PubMed]
19. Carslaw, H.S. *Introduction to the Mathematical Theory of the Conduction of Heat in Solids*; Macmillan and Company, Limited: London, UK, 1906.
20. Del Piero, G. A mechanical model for heat conduction. *Contin. Mech. Thermodyn.* **2020**, *32*, 1159–1172. [CrossRef]
21. Lee, M.H. Grid Independence Test of Computational Fluid Dynamics Model for Indoor Airflow Analysis. *Korean Inst. Archit. Sustain. Environ. Build. Syst.* **2020**, *14*, 183–194. [CrossRef]
22. Wang, Q.; Xia, S.N.; Yan, R.; Sun, D.-J.; Wan, Z.-H. Non-Oberbeck-Boussinesq effects due to large temperature differences in a differentially heated square cavity filled with air. *Int. J. Heat Mass Transf.* **2018**, *128*, 479–491. [CrossRef]

23. Chenoweth, D.R.; Paolucci, S. Natural convection in an enclosed vertical air layer with large horizontal temperature differences. *J. Fluid Mech.* **1986**, *169*, 173–210. [CrossRef]
24. Prasopchingchana, U. Investigation of solution differences on natural convection in a tall cavity simulated by using the Boussinesq approximation and the real air density equation. *IOP Conf. Ser. Mater. Sci. Eng.* **2021**, *1109*, 012046. [CrossRef]
25. Pourhemmati, S.; Mohammed, H.A.; Shafieian, A. The use of variable coil pitch of helical tube on the hydro-thermal performance improvement. *Case Stud. Therm. Eng.* **2023**, *53*, 103944. [CrossRef]
26. Singh, H.; Ichiyanagi, M.; Suzuki, T. Influence of Coil Pitch on Thermo-Fluid Characteristics for Square Channel Spiral Coil Sub-Cooled Condenser. *Int. J. Automot. Eng.* **2019**, *10*, 266–273. [CrossRef] [PubMed]
27. Xia, Z.; Gan, J.; Xia, H.; Chen, M.; Tang, R. Design and temperature uniformity optimization of electromagnetic heating hot plate for tire vulcanizing machine. *Energies* **2025**, *18*, 2695. [CrossRef]
28. Hassen, A.E.; Pagliano, L. Heat transfer characterization with alternative heating element layout in electric 'Injera' baking technology. *Results Eng.* **2023**, *19*, 101373. [CrossRef]
29. Vrábeľ, R. Optimum settings for discrete PID control of nonlinear systems. *Swarm Evol. Comput.* **2025**, *97*, 102052. [CrossRef]
30. *JJF 1637-2017*; Calibration Specification for Base Metal Thermocouples. China Quality Inspection Press: Beijing, China, 2017.
31. Shaikh, J.H.; Saha, K.; Talebbeydokhti, P.; Stoecki, S. Lidded SiP module: Warpage reduction techniques and thermal regime map. *Microelectron. Reliab.* **2025**, *169*, 115727. [CrossRef]
32. Jackson, A.; USDOE Office of Energy Efficiency and Renewable Energy (EERE); Arnold, R.L. *Investigating Temperature Uniformity and Accuracy in PV Module Lamination: A Verification Study*; National Renewable Energy Laboratory: Applewood, CO, USA, 2026.

Disclaimer/Publisher's Note: The statements, opinions and data contained in all publications are solely those of the individual author(s) and contributor(s) and not of MDPI and/or the editor(s). MDPI and/or the editor(s) disclaim responsibility for any injury to people or property resulting from any ideas, methods, instructions or products referred to in the content.